



Auroral ion acoustic wave enhancement observed with a radar interferometer system

N. M. Schlatter¹, V. Belyey², B. Gustavsson², N. Ivchenko¹, D. Whiter³, H. Dahlgren^{1,3}, S. Tuttle³, and T. Grydeland⁴

¹School of Electrical Engineering, Royal Institute of Technology, Stockholm, Sweden

²Department of Physics, University of Tromsø, Tromsø, Norway

³School of Physics and Astronomy, University of Southampton, Southampton, UK

⁴Northern Research Institute, Tromsø, Norway

Correspondence to: N. M. Schlatter (nmsc@kth.se)

Received: 8 February 2015 – Revised: 5 May 2015 – Accepted: 10 June 2015 – Published: 20 July 2015

Abstract. Measurements of naturally enhanced ion acoustic line (NEIAL) echoes obtained with a five-antenna interferometric imaging radar system are presented. The observations were conducted with the European Incoherent SCATter (EISCAT) radar on Svalbard and the EISCAT Aperture Synthesis Imaging receivers (EASI) installed at the radar site. Four baselines of the interferometer are used in the analysis. Based on the coherence estimates derived from the measurements, we show that the enhanced backscattering region is of limited extent in the plane perpendicular to the geomagnetic field. Previously it has been argued that the enhanced backscatter region is limited in size; however, here the first unambiguous observations are presented. The size of the enhanced backscatter region is determined to be less than 900×500 m, and at times less than 160 m in the direction of the longest antenna separation, assuming the scattering region to have a Gaussian scattering cross section in the plane perpendicular to the geomagnetic field. Using aperture synthesis imaging methods volumetric images of the NEIAL echo are obtained showing the enhanced backscattering region to be aligned with the geomagnetic field. Although optical auroral emissions are observed outside the radar look direction, our observations are consistent with the NEIAL echo occurring on field lines with particle precipitation.

Keywords. Ionosphere (Auroral ionosphere)

1 Introduction

Naturally enhanced ion acoustic lines (NEIALs) are anomalous radar echoes occasionally observed with incoherent

scatter radars, primarily during auroral precipitation (e.g., Sedgemore-Schulthess and St. Maurice, 2001). The enhanced backscatter can reach several orders of magnitude above the thermal backscatter and is thought to occur due to enhanced levels of ion acoustic wave activity (e.g., Sedgemore-Schulthess and St. Maurice, 2001). Explanations of the physical cause of NEIALs include streaming instabilities (Rietveld et al., 1991; Wahlund et al., 1992), decay from electrostatic ion-cyclotron waves (Bahcivan and Cosgrove, 2008), and Langmuir turbulence (e.g., Forme, 1993; Guio and Forme, 2006) driven by electron beams. Observations of NEIALs reported in recent years favors the Langmuir turbulence as a model to describe the echoes. Using interferometric observations, Grydeland et al. (2003) argued that the NEIAL backscatter region is limited to hundreds of meters in the plane perpendicular to the magnetic field and Grydeland et al. (2004) showed that the enhanced down- and upshifted ion line backscatter arise from the same volume. Observations of enhanced plasma lines occurring simultaneously to NEIALs (e.g., Strømme et al., 2005; Isham et al., 2012) can only be explained by Langmuir turbulence wave–wave interactions. Precipitation of electrons drives Langmuir waves via beam instability. Consecutive decay of the primary Langmuir waves into counter-streaming Langmuir waves and ion acoustic waves then leads to the enhanced ion acoustic wave activity.

An important step to advance the understanding of the instability criteria is to correlate the NEIAL echoes with the optical data. Based on optical data, the energy spectrum of electron precipitation can be derived (e.g., Lanchester and Gustavsson, 2013), something which is not possible with the

anomalous radar data. The horizontal size of the enhanced backscatter volume in the direction along the antenna baseline was shown (Grydeland et al., 2003, 2004) to be a few hundred meters or less based on the very high coherence of NEIALs observed with the two radar dishes at the EISCAT Svalbard facility. These results emphasize the necessity to determine the location of the anomalous echoes to relate NEIALs to particular auroral signatures and deduce further conditions of the instability criteria.

The technique used in incoherent scatter radar (Evans, 1969) experiments has been advanced to measure properties of the ionospheric plasma with high range resolution by introducing modulations of the transmitted radar wave such as alternating codes (Lehtinen and Häggström, 1987). In standard radar experiments used at EISCAT, the range resolution is a few kilometers down to hundreds of meters. However, the resolution perpendicular to the beam is limited by the antenna aperture. At ionospheric altitudes, the radar beam diameter is typically several kilometers. Beam swinging techniques, to resolve horizontal structure, are of limited use for a large variety of phenomena due to non-stationarity and sporadic occurrence. NEIALs is one such phenomenon. Radar interferometry yields samples of the 2-D Fourier transformation of the backscatter structure perpendicular to the beam, which can be estimated using aperture synthesis (e.g., Hysell and Chau, 2006).

In this report we present the first results obtained at the EISCAT Svalbard facility using aperture synthesis imaging methods. The interferometer system consists of the two EISCAT dish-antennas and three 4×4 phased-array antennas, and was designed for observations of strong backscatter targets such as meteors, NEIALs, and mesospheric clouds (polar mesospheric summer echoes). Here, we show results from observations of a NEIAL echo using four interferometric baselines.

2 Instrumentation and experiment

Two radar dishes were operated at the EISCAT Svalbard radar facility (78.15° N and 16.01° E) on 17 December 2012. Both dishes were pointed along the direction of the geomagnetic field corresponding to an elevation of 81.6° and azimuth of 184.5° E of north.

In addition to the two large aperture dish antennas, three small phased array receivers were used. Each receiver consists of 16 TV-transmitter-type panel antennas arranged in a 4×4 configuration on a rigid frame. The pointing direction of these antennas is fixed in the direction of the geomagnetic field. Figure 1a depicts the location of the receiver antennas relative to the position of the 42 m dish.

For the experiment reported herein a standard EISCAT alternating phase code (Lehtinen and Häggström, 1987) was run with the 42 m antenna as the transmitting antenna at a frequency of 500.3 MHz. The code has 30 bits with a bit length

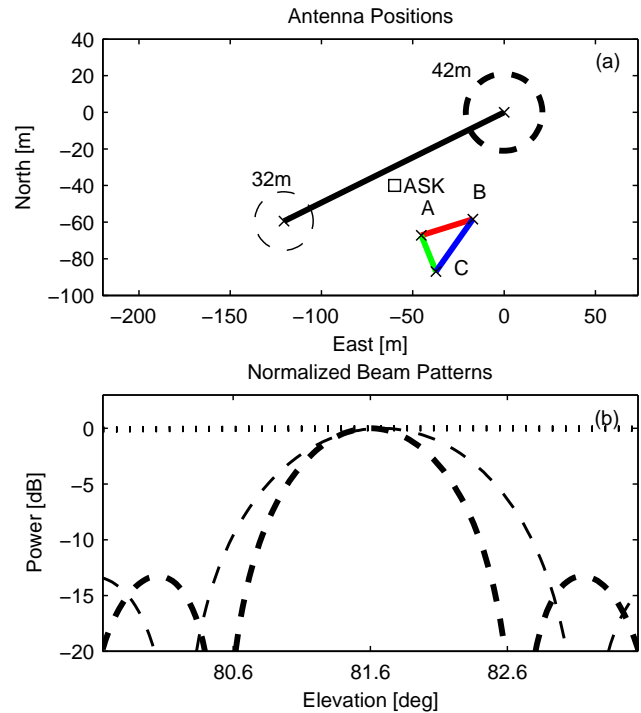


Figure 1. Receiver antennas at the EISCAT Svalbard Radar (ESR). Panel (a) shows the location of the receiver antennas relative to the position of the 42 m dish. Baselines employed for the analysis are indicated by lines (black, red, and green) connecting the involved antennas. The position of the ASK instrument is indicated by a square. Panel (b) depicts the normalized antenna beam patterns: 42 m as thick dashed line, 32 m dashed line, and the phased array receivers with nearly uniform patterns as dotted line.

of $50 \mu\text{s}$. During a full code cycle, lasting for 0.4 s, 64 pulses were transmitted. In receiving, the down-converted signal is sampled at a lag fractionality of 2 (Huuskonen et al., 1996), i.e., sampled at intervals of $25 \mu\text{s}$, giving a range resolution of 3.75 km. Both in-phase and quadrature samples are taken, giving a bandwidth of 40 kHz. On the array receivers only every second pulse was sampled due to a problem with the trigger for data acquisition. The raw voltage samples were saved from all five receivers for interferometric analysis.

The array receiver antennas A, B, and C were sampled on a separate receiver system from the EISCAT Svalbard Radar (ESR) 32 and 42 m antennas. A numerical oscillator which had not been set correctly in the radar experiment caused the phase of the two receiver systems to drift with respect to each other. The array receiver antennas were, thus, not sampled coherently with respect to the ESR dish antennas. As a result, the baselines which involve one ESR dish and one array receiver are omitted in the analysis and discussion. The lack of these baselines reduces the resolution of the radar interferometer. Cross-correlation estimates for the 32 m/42 m baseline and all combinations of antennas A, B, and C are not affected since the signals for these baselines were sampled

coherently. The four baselines employed for interferometry are indicated in Fig. 1a.

The Auroral Structures and Kinetics (ASK, e.g., Lanchester et al., 2009) optical instrument is co-located with the EISCAT Svalbard radar facility. ASK operates three imagers observing in the direction of the geomagnetic field. Each channel is equipped with a narrow bandwidth filter to measure auroral emissions at 6730, 7320, and 7774 Å. The imagers operate at 32 frames per second. Here, we present data obtained with the 6730 Å filter for the N21P band emission excited by high-energy electron precipitation (ASK1, e.g., Ashrafi et al., 2009) and the 7774 Å filter observing emission from atomic oxygen excited by low-energy electron precipitation (ASK3, e.g., Lanchester et al., 2009). The field of view of these imagers is $6.2 \times 6.2^\circ$ and is centered at magnetic zenith.

3 Method

In post processing the raw data are decoded and estimates of the auto- and cross-correlation functions for each antenna and antenna pair are formed as described by Grydeland et al. (2004). Time integration of the correlation estimates and Fourier transformation gives the power spectra \hat{S}_l and complex cross-spectra $\hat{S}_{l,m}$, where the indices denote the involved receivers. From these spectra, the cross-coherence values are computed:

$$\hat{V}_{l,m} = \frac{\hat{S}_{l,m}}{\sqrt{\hat{S}_l - N_l} \sqrt{\hat{S}_m - N_m}}, \quad (1)$$

where the N_l are the corresponding noise power spectral density estimates of the two receivers.

In aperture synthesis imaging the variation of scattered power density in the plane perpendicular to the beam is estimated from the cross-coherence measurements. The measurements are samples, depending on the baseline geometry, of the 2-D Fourier spectrum of the backscatter structure and define the so-called image which is computed by the use of inverse methods. The image is the backscatter power distribution as a function of look direction.

The forward model relates the complex cross-spectral measurements V with the backscatter cross section B , where B is a function of the look direction defined by the unit vector s . Each baseline is defined by the separation \mathbf{b} of the two receivers and the two antenna patterns A_l and A_m . The forward model is given by (Thompson et al., 1986):

$$V(k\mathbf{b}) = \int_{4\pi} A_N(s) B(s) \exp(jk\mathbf{b} \times s) d\Omega. \quad (2)$$

Here, k is the radar wavenumber, A_N the normalized two-way antenna pattern, and the integration is over the sphere. The antenna patterns are plotted in Fig. 1b. The product of

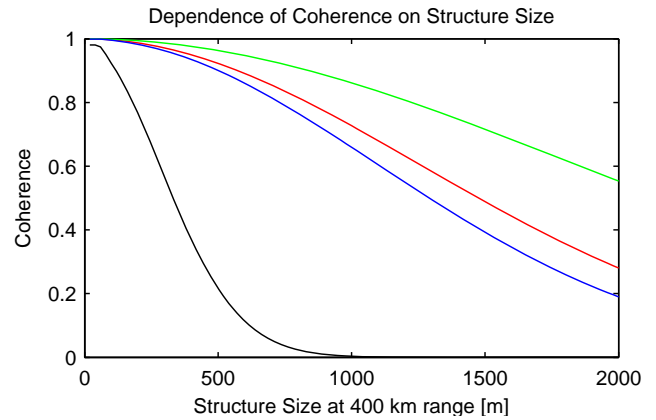


Figure 2. Dependence of coherence on the scale size of a scattering region with Gaussian cross section for the four baselines. Colors are the same as in Fig. 1. Note that the cut-off at 100 m in the coherence of 32 m/42 m baseline is due to the resolution of the model point grid.

the beam pattern of the transmitting antenna A_{42m} , common to all observations, and the backscatter cross section give the normalized backscattered power density $F = A_{42m}B$ which is the function to be derived from the measurements. The discretized forward model can be written as

$$V_n = \sum_i \sqrt{A_l A_m} \exp(jk\mathbf{b}_n \times s_i) f_i = \sum_i h_{i,n} f_i, \quad (3)$$

where i denotes a particular look direction, n is the baseline which involves receivers l and m , columns of $h_{i,n}$ are the impulse response, and f_i is the backscattered power distribution to be derived. In the numerical implementation, the above equation is replaced by two equations: one for the real part and one for the imaginary part. The coherence data used for imaging include the zero baseline, i.e., $\mathbf{b} = 0$, with an auto-coherence of 1.

For the discretization of s_i we use the look directions of the ASK1 pixels within 1.1° of the transmitting antenna beam center. The angular spacing of this grid is 1.5 arc min. The size of scattering structures resolved in the images is, however, determined by the baseline geometry and inversion method used.

In Fig. 2, the absolute value of coherence is plotted as a function of the size of the scatter target for the four baselines. A scatter target, centered to the pointing direction of the 42 m antenna, with a Gaussian scattering cross section was used to compute the coherence values. Backscatter targets smaller than 1.5 arc min are not resolved by the model. As a result a cut-off in the 32 m/42 m coherence is noticeable in Fig. 2 for small scatterer sizes. This cut-off does not affect the results discussed hereafter.

To compute the images a generalized Tikhonov regularization is used where $\|h \cdot f - V\|^2 + \lambda^2 \|f - f_0\|^2$ is the function to be minimized. Here, λ is a regularization parameter, chosen to be 50, and f_0 is the expectation value of the backscat-

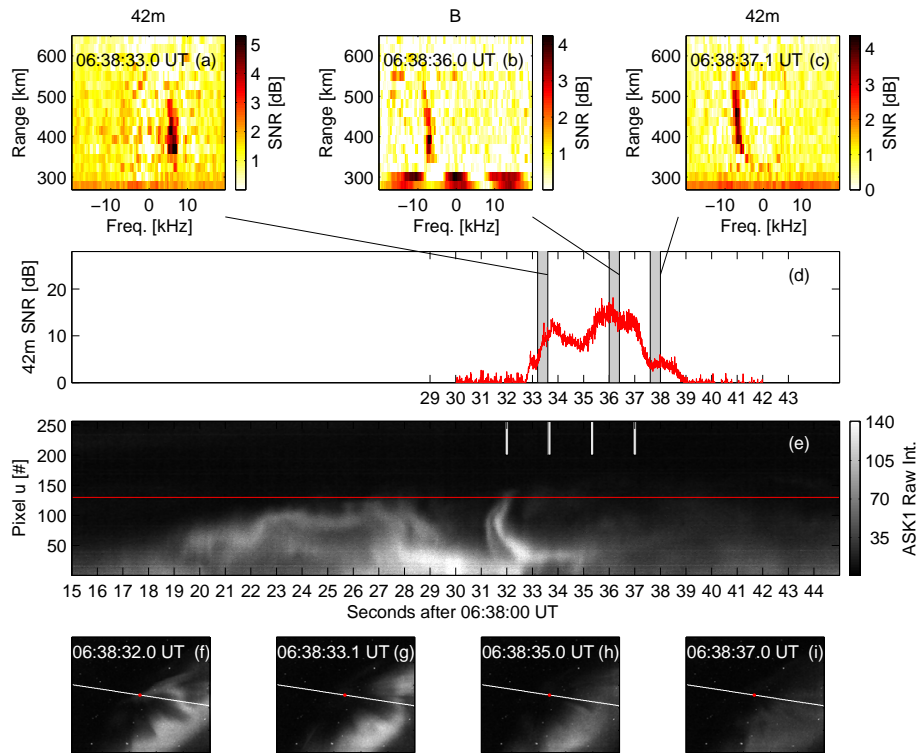


Figure 3. Time history for the NEIAL event observed on 17 December 2012. Panel (a)–(c) show power spectra (400 ms time integration and 22.5 km range gates) obtained with antenna 42 m, B, and 42 m again for the time periods highlighted in panel (d) and centered at 06:38:33.4, 06:38:36.2, and 06:38:37.8 UT. Measurements below 300 km are dominated by ground clutter. Panel (d) shows the signal-to-noise ratio (SNR) of unprocessed and un-decoded data observed with the 42 m antenna. Panel (e) shows a stackplot of intensity as observed with ASK1 along the white line in the snapshots presented in panel (f)–(i), the timing of which is indicated by the white tick marks. The solid red line, panel (e), and red markers, panels (f)–(i), indicate magnetic zenith.

ter distribution. The backscatter power distribution resulting from a uniform scattering cross-section was used as the expectation value.

Calibration of phase offsets introduced in the receiver systems is a crucial step before radar imaging can be achieved (Chau et al., 2008). At high latitudes, satellites transiting the radar beam provide strong backscattering targets which make it possible to estimate the receiver phase offsets and the antenna baselines. Here, we have used the method by Schlatter et al. (2013) to self-consistently solve for the baseline geometry and the phase offsets have been derived accordingly from satellite backscatter.

4 Observations

On 17 December 2012, NEIALs powerful enough to be observed in all five receiver antennas were recorded. During the NEIAL echoes, an auroral arc was observed close to magnetic zenith. An overview of the radar and optical observations is shown in Fig. 3. Enhanced backscattered radar power was observed between 06:38:32 and 06:38:39 UT at the ion acoustic frequencies with the 42 m antenna (panel

a and c) as well as with the additional receivers (panel b). The ion line spectra were asymmetric during the event period. First, the upshifted ion line shoulder was strongest and later, during the largest backscatter enhancements, the downshifted ion line shoulder was enhanced. The time history of power received with the 42 m dish is plotted in panel (d). Auroral emissions observed with ASK1 peaked at 06:38:30 UT as an auroral arc was moving into the field of view of ASK1. Figure 3e shows a keogram of ASK1 intensities observed along the white line plotted in ASK1 images displayed in panels (e)–(i). The 6730 Å emission observed by ASK1 is a prompt emission representative of the spatiotemporal behavior of particle precipitation. Along the arc, small-scale structures and rays were observed, and indicate the direction of the magnetic field. Variations in the brightness are noticeable in panels (e)–(i) close to the line along which the keogram is taken. After 06:38:34 UT optical emissions decreased and the arc moved outside the ASK field of view at around 06:38:45 UT.

The strongest backscatter was observed at around 06:38:36 UT with primarily the down-shifted ion line shoulder being enhanced. Figure 4 shows the power observed at the down-shifted ion line frequency in panel (a). Estimates

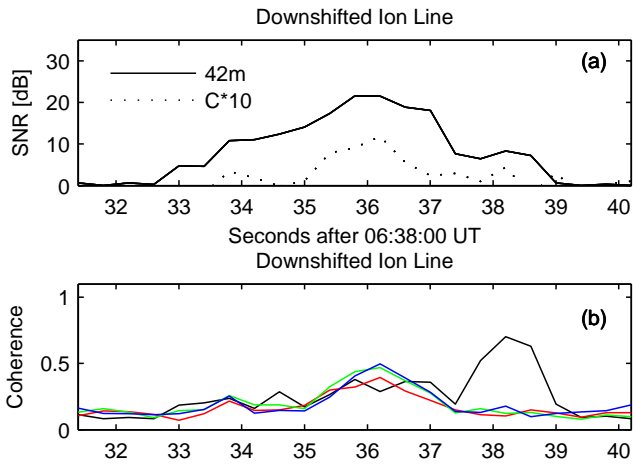


Figure 4. Time history of received power and coherence at 400 km range with 45 km range and 400 ms time integration. Panel (a) shows the SNR of the down-shifted ion line observed with the receivers 42 m and C. For better visibility of the curve the SNR of receiver C was multiplied by a factor of 10 dB. Panel (b) shows the coherence of the down-shifted ion line as observed with the 42–32 m receiver pair (black) and all three combinations of receivers A, B, and C where the color annotation is the same as in Fig. 1.

of the coherence magnitude, without noise subtraction, are shown in panel (b) for the 32 m/42 m baseline and all combinations of receivers A, B, and C.

Coherence in the phased array receiver baselines peaked at the time at which the highest power was observed with these receivers. Coherence values of about 0.4 were observed. Since noise was not subtracted, these values underestimate the coherence in the backscatter. At the same time the coherence in the longest baseline, 32 m/42 m, with the most sensitive receivers was at levels just below 0.4. Upon interpreting the coherence in terms of the scale size of the enhanced backscatter region (Fig. 2), we find that this value corresponds to below 500 m for the given altitude and in the baseline direction. A scatterer of this size should give a coherence of above 0.9 in the phased array baseline which is nearly parallel to 32 m/42 m, i.e., in A/B (red curve). With noise subtraction, the coherence estimates during this time period reach nearly 0.9 as expected from the 32 m/42 m observation with more sensitive receivers. Estimates of the coherence magnitude with noise subtraction are plotted in Fig. 5. Noise subtraction, however, can lead to unphysical coherence values of larger than unity at times when there was no signal. These times are disregarded.

Coherences observed in the array receiver baselines for the down-shifted ion line shoulder were between 0.34 and 0.92 during the time period of 06:38:34–06:38:37 UT. The coherence values during this time period correlate well with the observed power. Thus, the dip in coherence close to 06:38:34 UT was arguably caused by a decrease in signal

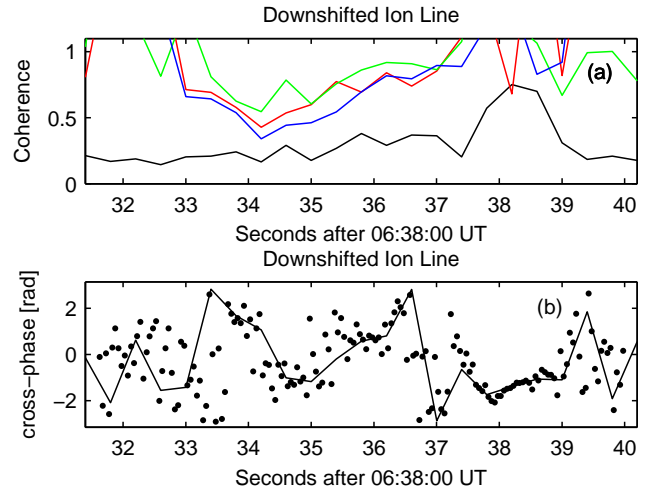


Figure 5. Coherence estimates with noise subtraction and cross-phase history at 400 km range with 45 km range and 400 ms time integration. In panel (a) the coherence estimates are plotted where colors are as in Fig. 1. In panel (b) the cross-phase for the 32 m/42 m baseline is shown. In addition to the 400 ms integrated cross-phase (black solid line) 50 ms integrated data are plotted (black dots).

quality rather than by an increase in size of the enhanced backscatter region.

Comparing the coherence values to the curves in Fig. 2, showing coherence as a function of scatterer size, yields estimates of the scale size of the enhanced backscatter region. Coherence values observed around 06:38:36 UT, i.e., the time at which the highest coherence was observed in the array baselines, correspond to a structure extended roughly 900 m in the north–south direction and 500 m in the east–west direction during the 0.4 s integration period. The highest coherence was observed in the 32 m/42 m baseline at 06:38:38 UT, reaching a value of 0.75 corresponding to about a 250 m scale size. At this time, the power in the phased array receivers was small and no meaningful conclusions can be drawn with respect to scale size perpendicular to 32 m/42 m.

The data discussed are time integrated. Time integration reduces the coherence in case of a moving scattering source. The estimates of scale size are, thus, not estimates of the instantaneous scale size, but the time-averaged scale size. Motion of the scattering source reflects in a variation of the cross-phase ϕ given by

$$\frac{d\phi}{dt} = k\mathbf{b} \cdot \frac{ds}{dt}, \quad (4)$$

where s is a unit vector pointing from the receivers towards the scattering source. The measured cross-phase is plotted in Fig. 5 for the 32 m/42 m baseline. At the time at which the highest coherence is observed in the 32 m/42 m baseline, the cross-phase varies gradually at a rate of about 0.8 rad s^{-1} at an altitude of 400 km. Thus, the angle of arrival shifts 0.035 deg s^{-1} , corresponding to a horizontal motion of the

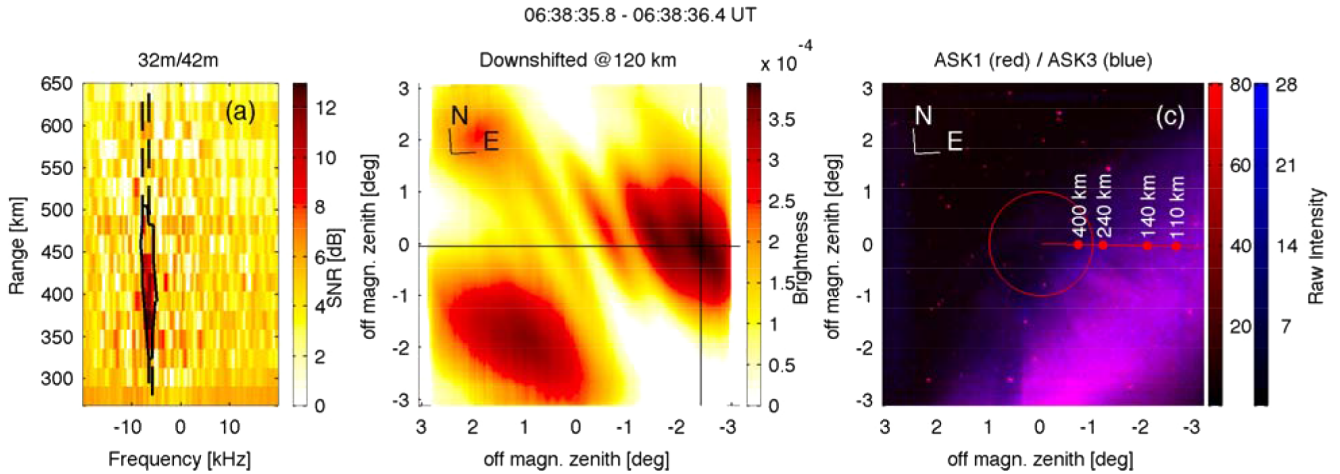


Figure 6. Radar and optical data for the time period 06:38:35.8–06:38:36.4 UT. Panel (a) shows the magnitude of the cross-spectrum of the 32 m/42 m baseline at 600 ms time integration and range gates of 22.5 km. The down-shifted ion line backscatter distribution mapped to an altitude of 120 km is shown in panel (b). The north and east directions are depicted in the upper left corner of the panel. Panel (c) shows a false color image of combined ASK1 and ASK3 data integrated over the same time period. The red circle indicates the main lobe of the 42 m antenna. The red line indicates the magnetic field line passing through the maximum backscattered power in (b). Tick marks along the field line indicate altitude.

enhanced backscattering region of 240 m s^{-1} in the direction of the 32 m/42 m baseline direction (west-southwest). During one integration period, lasting 0.4 s, the displacement is about 95 m. Therefore, the upper limit of the instantaneous scattering scale size, in the direction of the 32 m/42 m baseline, can be estimated to be 160 m during the time period discussed here.

In aperture synthesis imaging the scale size of backscatter features resolved in the images is determined by the baseline geometry (see Fig. 2) and inversion technique. The direction of highest resolution is in the direction of the longest baseline, corresponding to the 32 m/42 m baseline. Only short baselines constrain the image perpendicularly, resulting in poor resolution.

Sidelobes in the radar images occur at fixed angular distance, determined by the baseline geometry, to a scatter target. Sidelobes perpendicular to the 32 m/42 m baseline and within the transmitter beam are almost completely suppressed for the given baseline geometry. However, in the 32 m/42 m baseline direction, the direction of highest resolution, sidelobes are expected due to the limited number of baselines which constrain the radar images. For scatter targets elongated along the geomagnetic field these sidelobes can be reduced by averaging radar images along the geomagnetic field.

The spatial backscatter distribution is computed for the down-shifted ion line shoulder for the time period 06:38:35.8 to 06:38:36.4 UT. During this time period, the down-shifted ion line shoulder was enhanced and little power was observed in the upshifted ion line. Figure 6 shows the magnitude of the 32 m/42 m cross-spectrum in panel (a). The spectral region used for imaging is highlighted by the black line and has

been chosen using a threshold of long time integrated spectra. For altitudes with little backscattered power the spectral region defined by the black dashed line was chosen for imaging. Radar images are computed for each range gate of the radar data. The images are then mapped along the magnetic field to a reference altitude of 120 km. A mean image, i.e., the average backscattered power, is computed from all the images and displayed in panel (b) for look directions limited by the ASK field of view. The altitude of 120 km was chosen to match the auroral altitude. The maximum backscattered power, highlighted by two black lines, is observed approximately 2.5° E and 0.3° S of the 42 m beam center. Panel (c) of the same figure shows a false color image of ASK1 and ASK3 optical data integrated over the same time period. An auroral arc was observed in the southeast corner of the image apparently outside the radar main lobe indicated by a red circle. The red line indicates the field line passing through the maximum backscattered power in panel (b). Note here that the radar beam is defined by its angular width which is constant for all altitudes. Since the optical instrument is co-located with the radar, the size and position of the radar beam mapped to the optical data is independent of altitude. However, the horizontal beam width, measured in meters, linearly increases with altitude. Therefore, the field line indicated in panel (b) is within the radar beam for altitudes above 250 km and outside the radar beam for altitudes below. Figure 7, which is discussed below, visualizes these geometry considerations.

Beam cross-sections, along the black lines in Fig. 6b, of the down-shifted ion line backscatter and obtained for the same time period as data discussed above, are shown in Fig. 7. The geometry in the plots is such that the geomag-

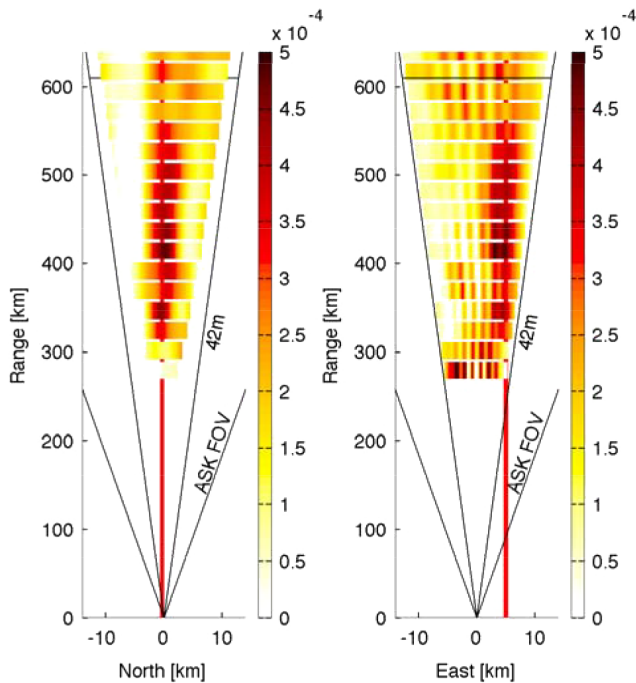


Figure 7. Beam cross-sections of the backscatter distribution derived for the down-shifted ion line shoulder. The red vertical line indicates the magnetic field close to the region from which enhanced backscatter is thought to arise and corresponds to the field line displayed in Fig. 6c.

netic field is in the vertical direction and the field of view of the optics and the transmitting antenna are shown for reference. A structure aligned with the geomagnetic field is seen between about 300 and 530 km range and highlighted with a vertical red line. The structure is pronounced at altitudes with high coherence values, while at other altitudes a more smooth backscatter distribution is obtained as expected. Other less-pronounced structures are sidelobes of the baseline geometry and occur at fixed angular distance to the enhanced backscatter volume and can therefore be regarded as an instrumental artifact. Note that the regularization in the inversion can be thought of as a filtering which causes the backscatter structure to appear larger in the images as compared to the backscatter scale size derived above.

5 Discussion

The limited spatial extent of the enhanced backscatter region of ion acoustic instability poses a major difficulty for trying to understand the driving mechanisms. For the event reported herein the radar measurements cover the region of enhanced backscatter only for altitudes above 300 km. Increased E- and F-region ionization caused by the particle precipitation occur outside the radar field of view. In fact, one could be misled by interpreting the single receiver radar data to try to under-

stand the driving mechanisms of ion acoustic instability for the event reported herein.

The magnetic field lines along which the enhanced backscatter is thought to have occurred is mapped to a region of optical emissions in ASK. However, the identified region is roughly 2.5° off-zenith (at 120 km altitude) and perspective effects need to be considered. Since the auroral arc was observed from the side no accurate measure of the arcs position with respect to the enhanced backscatter region can be derived here. It is therefore not possible to state whether the enhanced backscatter and optical emissions occur on the same field lines although it could be argued for it based on Fig. 6c.

Additional analysis of the presented data set is planned in order to investigate the spatial correlation of the echoes with the optical aurora. Such analysis requires modeling of the precipitation based on the optical observations and is beyond the scope of this article. Furthermore, the geometry based on the four baselines used herein constrain the image perpendicular to the 32 m/42 m poorly. The possibility of correcting for the unstable phase between the two receiver systems is being investigated. Such correction would allow one to employ the full set of 10 baselines for investigation of the NEIAL event.

6 Conclusions

Naturally enhanced ion acoustic echoes arise from a volume confined in the plane perpendicular to the magnetic field. For the reported event, we find the perpendicular size of the backscatter structure to be less than 900×500 m. Although optical emissions are observed outside the radar look direction, our observations are consistent with the enhanced ion acoustic echo to arise from field lines along which particle precipitation occurs.

Acknowledgements. EISCAT is an international association supported by research organizations in China (CRIRP), Finland (SA), Japan (NIPR and STEL), Norway (NFR), Sweden (VR), and the United Kingdom (NERC). The authors would like to acknowledge the EISCAT staff with special thanks to the staff at the EISCAT Svalbard site: Halvard Boholm, Espen Helgesen, and Assar Westman. Furthermore we would like to thank all those who have been involved in the EASI project.

The topical editor K. Hosokawa thanks B. Isham and another referee for help in evaluating this paper.

References

- Ashrafi, M., Lanchester, B. S., Lummerzheim, D., Ivchenko, N., and Jokiahho, O.: Modelling of N_2IP emission rates in aurora using various cross sections for excitation, *Ann. Geophys.*, 27, 2545–2553, doi:10.5194/angeo-27-2545-2009, 2009.

- Bahcivan, H. and Cosgrove, R.: Enhanced ion acoustic lines due to strong ion cyclotron wave fields, *Ann. Geophys.*, 26, 2081–2095, doi:10.5194/angeo-26-2081-2008, 2008.
- Chau, J. L., Hysell, D. L., Kuyeng, K. M., and Galindo, F. R.: Phase calibration approaches for radar interferometry and imaging configurations: equatorial spread F results, *Ann. Geophys.*, 26, 2333–2343, doi:10.5194/angeo-26-2333-2008, 2008.
- Evans, J.: Theory and practice of ionosphere study by Thomson scatter radar, *P. IEEE*, 57, 496–530, 1969.
- Forme, F. R. E.: A new interpretation on the origin of enhanced ion acoustic fluctuations in the upper ionosphere, *Geophys. Res. Lett.*, 20, 2347–2350, doi:10.1029/93GL02490, 1993.
- Grydeland, T., La Hoz, C., Hagfors, T., Blixt, E. M., Saito, S., Strømme, A., and Brekke, A.: Interferometric observations of filamentary structures associated with plasma instability in the auroral ionosphere, *Geophys. Res. Lett.*, 30, 1338, doi:10.1029/2002GL016362, 2003.
- Grydeland, T., Blixt, E. M., Løvhaug, U. P., Hagfors, T., Hoz, C. L., and Trondsen, T. S.: Interferometric radar observations of filamented structures due to plasma instabilities and their relation to dynamic auroral rays, *Ann. Geophys.*, 22, 1115–1132, doi:10.5194/angeo-22-1115-2004, 2004.
- Guio, P. and Forme, F.: Zakharov simulations of Langmuir turbulence: Effects on the ion-acoustic waves in incoherent scattering, *Phys. Plasmas*, 13, 122902, doi:10.1063/1.2402145, 2006.
- Huuskonen, A., Lehtinen, M. S., and Pirttilä, J.: Fractional lags in alternating codes: Improving incoherent scatter measurements by using lag estimates at noninteger multiples of baud length, *Radio Sci.*, 31, 245–261, doi:10.1029/95RS03157, 1996.
- Hysell, D. L. and Chau, J. L.: Optimal aperture synthesis radar imaging, *Radio Sci.*, 41, RS2003, doi:10.1029/2005RS003383, 2006.
- Isham, B., Rietveld, M. T., Guio, P., Forme, F. R. E., Grydeland, T., and Mjølhus, E.: Cavitating Langmuir Turbulence in the Terrestrial Aurora, *Phys. Rev. Lett.*, 108, 105003, doi:10.1103/PhysRevLett.108.105003, 2012.
- Lanchester, B. and Gustavsson, B.: Imaging of Aurora to Estimate the Energy and Flux of Electron Precipitation, *American Geophysical Union*, 171–182, doi:10.1029/2011GM001161, 2013.
- Lanchester, B. S., Ashrafi, M., and Ivchenko, N.: Simultaneous imaging of aurora on small scale in OI (777.4 nm) and N₂I_P to estimate energy and flux of precipitation, *Ann. Geophys.*, 27, 2881–2891, doi:10.5194/angeo-27-2881-2009, 2009.
- Lehtinen, M. S. and Häggström, I.: A new modulation principle for incoherent scatter measurements, *Radio Sci.*, 22, 625–634, doi:10.1029/RS022i004p00625, 1987.
- Rietveld, M. T., Collis, P. N., and St.-Maurice, J. P.: Naturally Enhanced Ion Acoustic Waves in the Auroral Ionosphere Observed with the EISCAT 933-MHz Radar, *J. Geophys. Res.*, 96, 19291–19305, doi:10.1029/91JA01188, 1991.
- Schlatter, N., Grydeland, T., Ivchenko, N., Belyey, V., Sullivan, J., Hoz, C. L., and Blixt, M.: Radar interferometer calibration of the EISCAT Svalbard Radar and a additional receiver station, *J. Atmos. Sol.-Terr. Phys.*, 105–106, 287–292, doi:10.1016/j.jastp.2012.11.017, 2013.
- Sedgemore-Schulthess, F. and St. Maurice, J.-P.: Naturally Enhanced Ion-Acoustic Spectra And Their Interpretation, *Surv. Geophys.*, 22, 55–92, doi:10.1023/A:1010691026863, 2001.
- Strømme, A., Belyey, V., Grydeland, T., La Hoz, C., Løvhaug, U. P., and Isham, B.: Evidence of naturally occurring wave-wave interactions in the polar ionosphere and its relation to naturally enhanced ion acoustic lines, *Geophys. Res. Lett.*, 32, L05103, doi:10.1029/2004GL020239, 2005.
- Thompson, A. R., Moran, J. R., and Swenson, G. W.: *Interferometry and Synthesis in Radio Astronomy*, John Wiley, Hoboken, N. J., 1986.
- Wahlund, J.-E., Forme, F. R. E., Opgenoorth, H. J., Persson, M. A. L., Mishin, E. V., and Volokitin, A. S.: Scattering of electromagnetic waves from a plasma: Enhanced ion acoustic fluctuations due to ion-ion two-stream instabilities, *Geophys. Res. Lett.*, 19, 1919–1922, doi:10.1029/92GL02101, 1992.